

Detections of [OIII] 88 μm in Two Quasars in the Reionization Epoch

Takuya Hashimoto^{1,2}, Akio K. Inoue¹, Yoichi Tamura³, Hiroshi Matsuo^{2,4}, Ken Mawatari⁵, and Yuki Yamaguchi⁶

¹Department of Environmental Science and Technology, Faculty of Design Technology, Osaka Sangyo University, 3-1-1, Nagaito, Daito, Osaka 574-8530, Japan

²National Astronomical Observatory of Japan, 2-21-1 Osawa, Mitaka, Tokyo 181-8588, Japan

³Division of Particle and Astrophysical Science, Graduate School of Science, Nagoya

⁴Department of Astronomical Science, School of Physical Sciences, The Graduate University for Advanced Studies (SOKENDAI), 2-21-1, Osawa, Mitaka, Tokyo 181-8588, Japan

⁵Institute for Cosmic Ray Research, The University of Tokyo, Kashiwa, Chiba 277-8582, Japan

⁶The University of Tokyo, 2-21-1 Osawa, Mitaka, Tokyo 181-0015, Japan

*E-mail: thashimoto@est.osaka-sandai.ac.jp

Received (reception date); Accepted (acceptation date)

Abstract

With the Atacama Large Millimeter/sub-millimeter Array (ALMA), we report detections of the far-infrared (FIR) [OIII] 88 μm line and the underlying dust continuum in the two quasars in the reionization epoch, J205406.48-000514.8 (hereafter J2054-0005) at $z = 6.0391 \pm 0.0002$ and J231038.88+185519.7 (hereafter J2310+1855) at $z = 6.0035 \pm 0.0007$. The [OIII] luminosity of J2054-0005 and J2310+1855 are $L_{[\text{OIII}]} = 6.8 \pm 0.6 \times 10^9 L_{\odot}$ and $2.4 \pm 0.6 \times 10^9 L_{\odot}$, corresponding to $\approx 0.05\%$ and 0.01% of the total infrared luminosity, respectively. Combining these [OIII] luminosities with [CII] 158 μm luminosities in the literature, we find that J2054-0005 and J2310+1855 have the [OIII]-to-[CII] luminosity ratio of 2.1 ± 0.4 and 0.3 ± 0.1 , respectively, the latter of which is the lowest among objects so far reported at $z > 6$. The high (low) luminosity ratio in J2054-0005 (J2310+1855) would be due to its stronger (weaker) UV stellar radiation field as implied from the high (low) dust temperature heated by star-formation activity, 50 ± 2 K (37 ± 1 K), which is estimated from the FIR spectral energy distribution.

Key words: quasars: general – galaxies: high-redshift – galaxies: ISM – galaxies: active

1 Introduction

Quasars are powered by supermassive black holes (SMBHs) with $\approx 10^8 - 10^{10} M_{\odot}$ (e.g., De Rosa et al. 2014; Wu et al. 2015). Owing to wide-area surveys, ≈ 100 quasars are discovered at $z > 6$ (e.g., Fan et al. 2003; Jiang et al. 2016; Mazzucchelli et al. 2017; Matsuoka et al. 2018) and up to $z = 7.54$ (Bañados et al. 2018). How SMBHs have accreted within ≈ 1 Gyr after the Big Bang is one of the most important question in modern astronomy (Valiante et al. 2017).

A variety of tracers are used to understand properties of quasars and their host galaxies at $z > 6$. Rest-frame far-infrared

(FIR) dust continuum observations show that high- z quasar host galaxies have star formation rates (SFRs) $\approx 50 - 2700 M_{\odot} \text{ yr}^{-1}$ and large dust masses $\approx 10^7 - 10^9 M_{\odot}$ (e.g., Venemans et al. 2018 and references therein). The carbon monoxide (CO) line observations reveal a large amount of gas mass in the host galaxies ($\approx 10^{10} M_{\odot}$) (e.g., Wang et al. 2010). The FIR fine structure line of [CII] 158 μm is widely used to obtain the precise redshift and the dynamical mass (e.g., Wang et al. 2013; Decarli et al. 2018; Izumi et al. 2018).

Combinations of FIR fine structure lines are useful to obtain physical properties of the interstellar medium (ISM) such

as the gas-phase metallicity, the electron density, and the ionization parameter (e.g., Nagao et al. 2011; Pereira-Santaella et al. 2017). Among the FIR lines, the [OIII] 88.356 μm line ($\nu_{\text{rest}} = 3393.006244$ GHz) would be a good next target after [CII] because it is the second most commonly observed line in normal star-forming galaxies at $z > 6$ (e.g., Inoue et al. 2016; Tamura et al. 2018). Indeed, recent ALMA observations demonstrate that [OIII] is detectable even at $z = 9.11$ (Hashimoto et al. 2018a).

In this letter, we report results of our ALMA Band 8 observations targeting [OIII] in two quasars at $z \approx 6$, J205406.48-000514.8 (hereafter J2054-0005) and J231038.88+185519.7 (J2310+1855). With our observations (§2), we successfully detect [OIII] and the underlying dust continuum (§3). In conjunction with [CII] measurements in the literature, we discuss their [OIII]-to-[CII] line luminosity ratios (§4). Throughout this paper, we adopt a flat Λ CDM cosmology ($\Omega_m = 0.272$, $\Omega_\Lambda = 0.728$, and $H_0 = 70.4$ km s $^{-1}$ Mpc $^{-1}$; Komatsu et al. 2011)

2 Our Sample and ALMA Band 8 Data

2.1 Sample

Among the $z > 6$ quasars, we have selected two FIR bright objects, J2054-0005 and J2310+1855, whose redshifts are suitable for [OIII] observations with ALMA. These objects are originally discovered by the Sloan Digital Sky Survey data (Jiang et al. 2008, 2016). J2054-0005 (J2310+1855) has the UV absolute magnitude of $M_{1450} = -26.1$ (-27.8) and the bolometric luminosity of $2.8 \times 10^{13} L_\odot$ ($9.3 \times 10^{13} L_\odot$) (Wang et al. 2013). The BH mass in J2054-0005 (J2310+1855) is estimated to be $0.9_{-0.6}^{+1.6} \times 10^9 M_\odot$ ($2.3_{-1.8}^{+5.1} \times 10^9 M_\odot$) (Willott et al. 2015). The [CII] redshift value of J2054-0005 (J2310+1855) is $z = 6.0391 \pm 0.0002$ (6.0031 ± 0.0002) (Wang et al. 2013).

2.2 Observations and Data

We performed observations of [OIII] with ALMA Band 8 during 2018 March and 2018 July (ID 2017.1.01195.S, PI: T. Hashimoto). In J2054-0005 (J2310+1855), 43 antennas with the baseline lengths of 15 – 785 m (15 – 360 m) were used, and the total on-source exposure time was 127 minutes (176 minutes). Four spectral windows (SPWs) with a bandwidth of 1.875 GHz were used in the Frequency Division Mode. Two slightly overlapping SPWs (0 & 1) were used to target [OIII], covering the frequency range of 480.71 – 483.68 GHz (483.19 – 486.31 GHz) for J2054-0005 (J2310+1855). The other two SPWs (2 & 3) were used to observe the continuum, covering 492.21 – 495.96 GHz (494.70 – 498.45 GHz) for J2054-0005 (J2310+1855). A quasar J1924-2914 (J2258-2758) was used for bandpass and flux calibrations, and a quasar

J2101+0341 (J2253+1608) was used for phase calibrations. The data were reduced and calibrated using CASA pipeline version 5.1.1-5. We produced images and cubes with the CLEAN task using the natural weighting. To create a pure dust continuum image, we collapsed all off-line channels. To create a pure line image, we subtracted continuum using the off-line channels in the line cube with the CASA task `uvcontsub`. In J2310+1855, we could not obtain the data product in SPW1 due to very strong atmospheric absorption¹.

With the CASA task `imstat`, we estimate the rms level of the continuum image of J2054-0005 (J2310+1855) to be 101 $\mu\text{Jy beam}^{-1}$ (362 $\mu\text{Jy beam}^{-1}$). The spatial resolution of the continuum image is $0''.38 \times 0''.34$ ($0''.69 \times 0''.60$) in FWHM with a beam position angle, PA, of 69° (-61°). The typical rms level of the line cube is 0.6 mJy beam $^{-1}$ (0.8 mJy beam $^{-1}$) per 30 km s $^{-1}$ bin.

3 Results

3.1 Dust Continuum

Our data probe dust continuum emission at the rest-frame wavelength, λ_{rest} , of ≈ 87 μm . The top left and bottom left panels of Figure 1 show dust continuum images of J2054-0005 and J2310+1855, respectively. Our measurements are summarized in Table 1.

J2054-0005– To estimate the flux density and the beam deconvolved size of the dust continuum, we apply the CASA task `imfit` assuming a 2D Gaussian profile for the specific intensity. We estimate the continuum flux density to be $S_{\nu, 87\mu\text{m}} = 10.35 \pm 0.22$ mJy. The beam deconvolved size is $(0.23 \pm 0.02) \times (0.15 \pm 0.02)$ arcsec 2 , corresponding to $(1.34 \pm 0.13) \times (0.88 \pm 0.13)$ kpc 2 at $z = 6.0391$, with PA = $177^\circ \pm 10^\circ$.

J2310+1855– The continuum flux density is 24.89 ± 0.72 mJy. The beam deconvolved size is $(0.31 \pm 0.05) \times (0.22 \pm 0.06)$ arcsec 2 , corresponding to $(1.81 \pm 0.29) \times (1.28 \pm 0.35)$ kpc 2 at $z = 6.0391$, with PA = $154^\circ \pm 32^\circ$.

These deconvolved size and PA values are consistent with those obtained by Wang et al. (2013) using ALMA Band 6 data within 1σ uncertainties.

3.2 [OIII] 88 μm

The [OIII] is detected in the two quasars. Our measurements are summarized in Table 1.

The top (bottom) middle panel of Figure 1 shows a velocity-integrated intensity image between 481.7 – 482.6 GHz (484.1 – 485.0 GHz) for J2054-0005 (J2310+1855). The peak intensity is 1.67 ± 0.10 Jy km s $^{-1}$ beam $^{-1}$ (0.94 ± 0.15 Jy km s $^{-1}$ beam $^{-1}$). We perform photometry on the image with

¹ According to the QA2 Report, ALMA staffs tried to keep a part of the data by changing parameters of the pipeline, but it did not work.

Table 1. Summary of observational results.

	J2054-0005	J2310+1855
$z_{[\text{OIII}]}$	6.0391 ± 0.0002	6.0035 ± 0.0007
FWHM([OIII]) [km s ⁻¹]	282 ± 17	333 ± 72
[OIII] integrated flux [Jy km s ⁻¹]	3.79 ± 0.34	1.38 ± 0.34
[OIII] luminosity [$10^9 L_{\odot}$]	6.79 ± 0.61	2.44 ± 0.61
$S_{\nu,87}$ [mJy]	10.35 ± 0.22	24.89 ± 0.72
Dust deconvolved size ^a [arcsec ²]	$(0.23 \pm 0.02) \times (0.15 \pm 0.02)$	$(0.31 \pm 0.05) \times (0.22 \pm 0.06)$
[OIII] deconvolved size ^a [arcsec ²]	$(0.49 \pm 0.07) \times (0.45 \pm 0.06)$	$(0.44 \pm 0.27) \times (0.38 \pm 0.13)$
T_d [K]	50 ± 2	37 ± 1
β_d	1.8 ± 0.1	2.2 ± 0.1
L_{TIR}^b [$10^{13} L_{\odot}$]	$1.3^{+0.2}_{-0.2}$	$1.9^{+0.2}_{-0.1}$
SFR _{IR} ^c [$M_{\odot} \text{ yr}^{-1}$]	1897^{+265}_{-216}	2873^{+294}_{-232}

Note. ^a The values represent major and minor-axis FWHM values of a 2D Gaussian profile. ^b The total luminosity, L_{TIR} , is estimated by integrating the modified-black body radiation at 8 – 1000 μm .

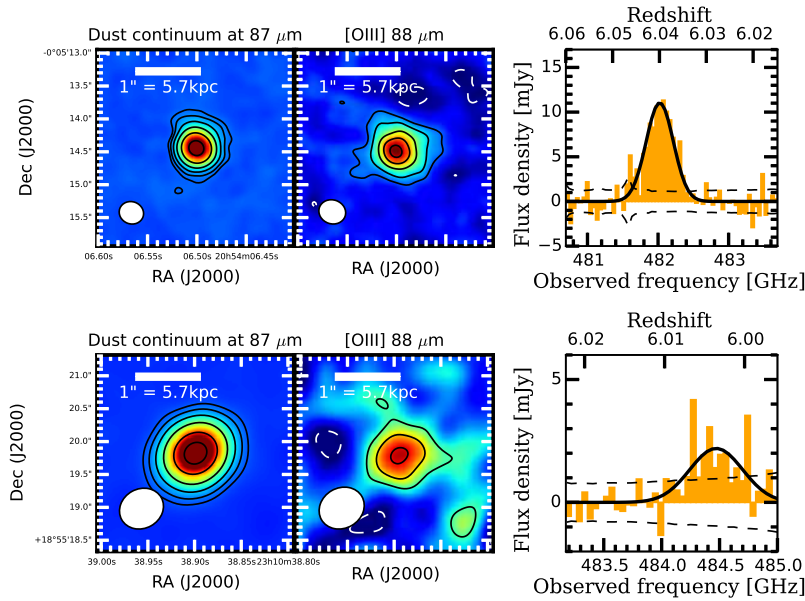


Fig. 1. The dust continuum image at $\approx 87 \mu\text{m}$ (left), the [OIII] $88 \mu\text{m}$ line image (middle), and the continuum-subtracted [OIII] spectrum (right). In the left and middle panels, the ellipse at lower left corner indicates the synthesized beam size of ALMA, and the scale bar is shown at the upper left corner. Negative and positive contours are shown by the white dashed and black solid lines, respectively. The continuum-subtracted [OIII] spectrum is extracted from the region with $> 3\sigma$ detections in the velocity-integrated intensity images. The black solid lines are the best-fit Gaussian for the [OIII] line, while the black dashed lines show the $\pm 1\sigma$ noise levels. **J2054-0005 (Top)**– The dust continuum contours drawn at $(-2, 2, 4, 8, 16, 32, 64) \times \sigma$, where $\sigma = 101 \mu\text{Jy beam}^{-1}$. The [OIII] line contours drawn at $(-2, 2, 4, 8, 12, 16) \times \sigma$, where $\sigma = 96 \text{ mJy beam}^{-1} \text{ km s}^{-1}$. **J2310+1855 (Bottom)**– The dust continuum contours at $\approx 87 \mu\text{m}$ drawn at $(-2, 2, 4, 8, 16, 32, 50) \times \sigma$, where $\sigma = 362 \mu\text{Jy beam}^{-1}$. The [OIII] line contours drawn at $(-2, 2, 4, 6) \times \sigma$, where $\sigma = 150 \text{ mJy beam}^{-1} \text{ km s}^{-1}$.

the CASA task `imfit` assuming a 2D Gaussian profile for the line intensity. In J2054-0005, the total line flux is estimated to be $3.79 \pm 0.34 \text{ Jy km s}^{-1}$. The beam-deconvolved size is $(0.49 \pm 0.07) \times (0.45 \pm 0.06) \text{ arcsec}^2$, corresponding to $(2.87 \pm 0.41) \times (2.63 \pm 0.35) \text{ kpc}^2$ at $z = 6.0391$, with PA = $75^\circ \pm 82^\circ$. While the [OIII] PA value is consistent with that of [CII], $91^\circ \pm 173^\circ$, within 1σ uncertainties, the size of the [OIII] emitting region may marginally larger than that of the [CII] emitting region, $(0.35 \pm 0.04) \times (0.32 \pm 0.05) \text{ arcsec}^2$ (Wang et al. 2013). In J2310+1855, the total line flux is estimated to be $1.38 \pm 0.34 \text{ Jy km s}^{-1}$. The beam-deconvolved size is $(0.44 \pm 0.27) \times (0.38 \pm 0.13) \text{ arcsec}^2$, corresponding

to $(2.57 \pm 1.58) \times (2.22 \pm 0.76) \text{ kpc}^2$ at $z = 6.0035$, with PA = $70^\circ \pm 97^\circ$. These size and PA values are consistent with those of [CII], $(0.56 \pm 0.03) \times (0.39 \pm 0.04) \text{ arcsec}^2$ and PA = $142^\circ \pm 10^\circ$, within 1σ uncertainties (Wang et al. 2013).

The top (bottom) right panel of Figure 1 shows the continuum-subtracted spectrum of J2054-0005 (J2310+1855) extracted from the [OIII] region with $> 3\sigma$ detections in the velocity-integrated intensity image. We obtain the [OIII] redshift of 6.0391 ± 0.0002 (6.0035 ± 0.0007) and the FWHM value of $282 \pm 17 \text{ km s}^{-1}$ ($333 \pm 72 \text{ km s}^{-1}$), which are consistent with the [CII] measurements (Wang et al. 2013). Based on a combination of the flux and redshift values, we obtain the

[OIII] luminosity of $6.76 \pm 0.61 \times 10^9 L_{\odot}$ ($2.44 \pm 0.61 \times 10^9 L_{\odot}$) in J2054-0005 (J2310+1855).

To investigate a possible broad velocity component in the [OIII] line, as that found in a $z = 6.4$ quasar in [CII] (Maiolino et al. 2012), we extract two additional spectra from the [OIII] regions with $> 1\sigma$ and $> 2\sigma$ detections in the velocity-integrated intensity images. We do not find any broad velocity component in the spectra.

We note that the two quasars have the [OIII] emitting region size of $\approx 2 - 3$ kpc (FWHM), which is significantly larger than the continuum emitting region size of ≈ 1 kpc (FWHM).

3.3 Tight Constraints on the Dust Temperature and the Infrared Luminosity

Previous studies have shown that FIR dust continuum emission of quasars at $\lambda_{\text{rest}} \gtrsim 50 \mu\text{m}$ is mainly powered by star-formation activity with negligible contribution from active galactic nuclei (AGNs) (Leipski et al. 2013). Assuming that FIR dust continuum emission is described as an optically-thin modified-black body radiation, $I_{\nu} \propto \nu^{3+\beta_d}/(\exp(h\nu/kT_d) - 1)$, we constrain the single dust temperature, T_d , and the dust emissivity index, β_d , of the two quasar host galaxies taking CMB effects into account (da Cunha et al. 2013) (Table 1).

In J2054-0005, we use four flux density measurements of 12.0 ± 4.9 mJy, 10.35 ± 0.22 mJy, 2.98 ± 0.05 mJy, and 2.38 ± 0.53 mJy obtained with Herschel 350 μm data (Leipski et al. 2013), our ALMA 488 GHz, ALMA 262 GHz data (Wang et al. 2013), and MAMBO 250 GHz data (Wang et al. 2008), respectively. These data sample $\lambda_{\text{rest}} \approx 50 - 200 \mu\text{m}$. By fitting modified-black body models corrected for the CMB effects to the photometry data, we obtain $T_d = 50 \pm 2$ K and $\beta_d = 1.8 \pm 0.1$ based on the χ^2 statistics. The best-fit model is shown in the left panel of Figure 2. Integrating the modified-black body radiation over $8 - 1000 \mu\text{m}$, we obtain the total infrared luminosity to be $L_{\text{TIR}} = 1.3_{-0.2}^{+0.2} \times 10^{13} L_{\odot}$. Following Kennicutt & Evans (2012) under the assumption of the Kroupa initial mass function (IMF; Kroupa 2001) in the range of $0.1 - 100 M_{\odot}$, we obtain the IR-based star formation rate (SFR_{IR}) $\approx 1900 M_{\odot} \text{yr}^{-1}$. Note our ALMA Band 8 data are useful to constrain T_d because the data probe the wavelengths close to the peak of the dust spectral energy distribution (SED).

Likewise, in J2310+1855, we use five flux density measurements of 24.89 ± 0.72 mJy, 8.91 ± 0.08 mJy, 8.29 ± 0.63 mJy, 0.40 ± 0.05 , and 0.41 ± 0.03 mJy obtained with our ALMA 488 GHz, ALMA 262 GHz data (Wang et al. 2013), MAMBO 250 GHz data, MAMBO 99 GHz data (Wang et al. 2008), and ALMA 91.5 GHz (Feruglio et al. 2018), respectively. These data sample $\lambda_{\text{rest}} \approx 90 - 500 \mu\text{m}$. We obtain $T_d = 37 \pm 1$ K, $\beta_d = 2.2 \pm 0.1$, $L_{\text{TIR}} = 1.9_{-0.1}^{+0.2} \times 10^{13} L_{\odot}$, and $\text{SFR}_{\text{IR}} \approx 2900 M_{\odot} \text{yr}^{-1}$ in the same way as in J2054-0005.

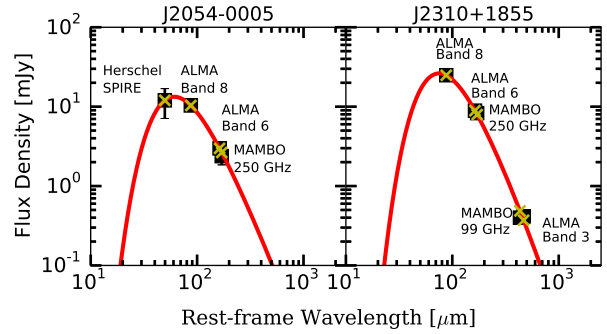


Fig. 2. Left and right panels show the FIR dust SED of J2054-0005 and J2310+1855, respectively. In each panel, black squares denote the measurements with error bars typically smaller than the symbols, while the best-fit data are shown in yellow crosses. The red line corresponds to the best-fit SED. See the text for the details of the data used in the fit.

These T_d and β_d values are within the ranges obtained in a mean SED of six quasar host galaxies at $z = 1.8 - 6.4$, $T_d = 47 \pm 3$ K and $\beta_d = 1.6 \pm 0.1$ (Beelen et al. 2006) and in a mean SED of seven quasar host galaxies at $z \approx 4 - 5$, $T_d = 41 \pm 5$ K and $\beta_d = 1.95 \pm 0.3$ (Priddey & McMahon 2001). Nevertheless, our results demonstrate the variety of dust properties on the individual basis. We use these T_d and SFR_{IR} values to interpret our results in §4.

3.4 Luminosity Ratios

Based on a compiled sample of local dwarf and spiral galaxies with high dynamic ranges in metallicity and L_{TIR} , Cormier et al. (2015) have shown that the [OIII]-to- L_{TIR} ratio anticorrelates with L_{TIR} , the so-called FIR line deficit (e.g., Malhotra et al. 1997; Díaz-Santos et al. 2017). The local galaxies have the [OIII]-to- L_{TIR} ratio ranging from $\approx 10^{-5}$ to $\approx 10^{-2}$. Recently, Tamura et al. (2018) have investigated the relation at higher- z based on a compiled sample of $z \approx 7 - 9$ galaxies, showing that at least high- z galaxies with dust continuum detections follow a similar relation as in the local Universe. Our two quasars are useful to further investigate the trend at the reionization epoch because of their high L_{TIR} values. The luminosity ratios are $\log(L_{\text{OIII}}/L_{\text{TIR}}) = -3.3 \pm 0.1$ and -4.0 ± 0.1 in J2054-0005 and J2310+1855, respectively. In the left panel of Figure 3, we plot the two quasars along with eight objects at $z > 7$ (see caption for the details) and lower- z objects. The latter includes various populations of local galaxies taken from the Herschel DGS (Cormier et al. 2015) and SHINING (Herrera-Camus et al. 2018) samples, local spirals (Brauer et al. 2008), and lensed sub-millimeter galaxies (SMGs) at $z \approx 1 - 4$ (Zhang et al. 2018). We confirm a trend that high- z objects follow a similar relation as in the local Universe *but* shifted toward higher L_{TIR} values (or higher [OIII]-to- L_{TIR} values). Such a shift toward higher L_{TIR} values is also found in the relation between [CII]-to- L_{TIR} and L_{TIR} (Stacey et al. 2010). Herrera-

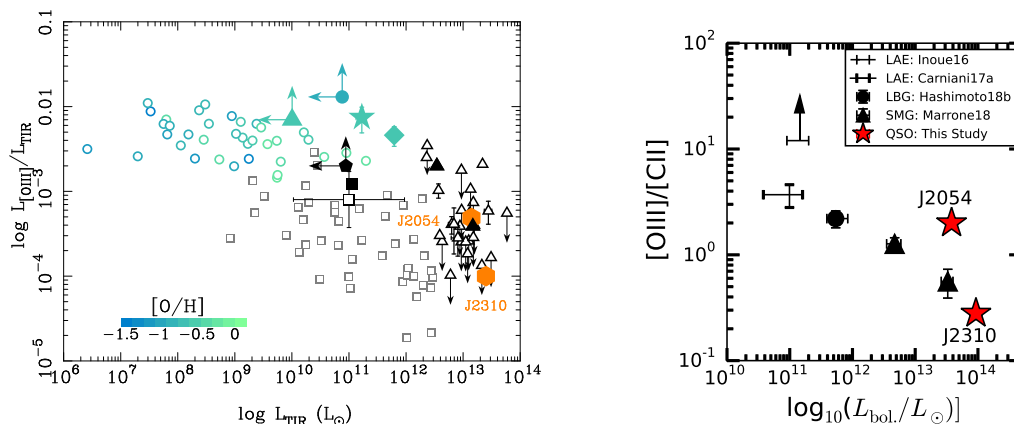


Fig. 3. (Left panel) The [OIII]-to- L_{TIR} ratio plotted against L_{TIR} , where the luminosities are corrected for magnification, if any. Orange hexagons show the two quasars. The other eight filled symbols represent $z \approx 7-9$ objects compiled by Tamura et al. (2018): SPT0311–58 E/W at $z = 6.90$ (triangles, Marrone et al. 2018); BDF-3299 at $z = 7.11$ (pentagon with two arrows, Carniani et al. 2017), B14-65666 at $z = 7.15$ (filled diamond, Hashimoto et al. 2018b), SXDF-NB1006-2 at $z = 7.21$ (circle with two arrows, Inoue et al. 2016), MACS0416.Y1 at $z = 8.31$ (five-pointed star, Tamura et al. 2018), A2744.YD4 at $z = 8.38$ (square, Laporte et al. 2017), and MACS1149-JD1 at $z = 9.11$ (triangle with two arrows, Hashimoto et al. 2018a). The open symbols show lower- z galaxies including the Herschel DGS (open circles, Cormier et al. 2015) and SHINING samples (thin open squares, Herrera-Camus et al. 2018), the median of local spirals (thick open square, Brauer et al. 2008), and $z \approx 2-4$ dusty star-forming galaxies with spectroscopic redshifts (open triangles, Zhang et al. 2018). For the $z > 6$ objects except for the two quasars and SPT0311–58 E/W, we have assumed $L_{\text{TIR}} = 50$ K and $\beta_d = 1.6$ for consistency. The blue-to-green color code shown for MACS0416.Y1, SXDF-NB1006-2, MACS1149-JD1, B14-65666 and local dwarfs indicates the best-fitting oxygen abundances. (Right panel) The [OIII]-to-[CII] luminosity ratio plotted against the bolometric luminosity at $z > 6$. The sample includes the two quasars (two red five-pointed stars); SPT0311–58 E/W (triangles); B14-65666 (circle); BDF-3299 (‘+’ symbol); and SXDF-NB1006-2 (‘-’ symbol with an upward arrow). The bolometric luminosity values of the two quasars are taken from the literature. Those of the other galaxies are obtained in Hashimoto et al. (2018b) as the summation of the UV luminosity and L_{TIR} , where we assume $L_{\text{TIR}} = 50$ K and $\beta_d = 1.6$ except for SPT0311–58 E/W. For the two LAEs with L_{TIR} upper limits, the lower limit corresponds to the UV luminosity, while the upper limit denotes the summation of the UV luminosity and the 3σ L_{TIR} upper limits.

Camus et al. (2018) show that the discrepancy between low and high- z objects disappears if one plots the [OIII]-to- L_{TIR} ratio against the IR surface brightness, Σ_{IR} , implying that the shift is due to the compactness of higher- z objects at a given L_{TIR} .

We next turn our attention to the [OIII]-to-[CII] luminosity ratio. Based on a compiled sample of five objects at $z \gtrsim 7$ with [OIII] and [CII] observations (Inoue et al. 2016; Carniani et al. 2017; Marrone et al. 2018), Hashimoto et al. (2018b) have demonstrated a trend that the [OIII]-to-[CII] line luminosity ratio becomes small if a galaxy has a large bolometric luminosity. Their sample includes two Ly α emitters (LAEs), one Lyman break galaxy (LBG), and two SMGs. Thus, J2054-0005 and J2310+1855 offers us an invaluable opportunity to investigate the line luminosity ratio in quasars at $z > 6$ for the first time. In J2054-0005 (J2310+1855), combining our [OIII] luminosity and the [CII] luminosity of $3.3 \pm 0.5 \times 10^9 L_{\odot}$ ($8.7 \pm 1.4 \times 10^9 L_{\odot}$) in Wang et al. (2013), we obtain the line luminosity ratio of 2.1 ± 0.4 (0.3 ± 0.1). The right panel of Figure 3 shows that quasars also follow the trend. Notably, J2310+1855 has the highest bolometric luminosity and the lowest [OIII]-to-[CII] ratio so far reported among objects at $z > 6$.

4 Discussion and Summary

To interpret [OIII] in quasars, we need to separate the [OIII] contribution from star formation and AGN activity. For the lat-

ter, [OIII] can arise from the Narrow Line Region (NLR) of AGNs because the NLR has a relatively small electron density of $100 - 300 \text{ cm}^{-3}$ (e.g., Bennert et al. 2006; Kakkad et al. 2018), which is smaller than the critical density of [OIII] $88 \mu\text{m}$ ($\approx 500 \text{ cm}^{-3}$). Indeed, the size of the [OIII] emitting region of the two quasars ($\approx 2 - 3$ kpc in FWHM) are reasonable for the size of stellar disks or extended NLRs. Ideally, one can separate the contribution based on spatially resolved diagnostics such as the BPT diagram (Baldwin et al. 1981) as performed in local Seyfert and LINER galaxies (Kakkad et al. 2018). However, it is difficult to separate the contribution based on the [OIII]-to-[CII] line ratio alone because it is insensitive to the presence of AGNs; Herrera-Camus et al. (2018) demonstrate that both star formation and AGN activity can reproduce the [OIII]-to-[CII] luminosity ratio of $\approx 0.1 - 2.0$ (see their Figure 11). Therefore, we instead examine if [OIII] luminosity-based SFRs (SFR_{OIII}) are comparable to SFR_{IR} values (Table 1). For the conversion of the [OIII] luminosity to the SFR, we use the empirical relation in the local Universe which assumes the Kroupa IMF in the range of $0.1 - 100 M_{\odot}$ (De Looze et al. 2014). The authors present different empirical relations for e.g., metal-poor dwarf galaxies, starburst, the composite of star formation and AGNs, ultraluminous infrared galaxies (ULIRGs), and the entire sample. In J2054-0005, SFR_{IR} and SFR_{OIII} values are consistent with each other within a factor of ≈ 2 if we use the templates for the entire, starburst, and AGN samples, implying that we cannot

determine the dominant contribution to [OIII]. In J2310+1855, on the other hand, the two SFR values are consistent with each other within a factor of ≈ 2 only if we use the template for the ULIRGs. We obtain $\text{SFR}_{\text{OIII}} \approx 500 M_{\odot} \text{ yr}^{-1}$ with the AGN template, a factor of ≈ 6 lower than SFR_{IR} , indicating that the AGN contribution may be small. For a definitive conclusion, the spatially resolved [OI] $63 \mu\text{m}$ -to-[CII] line ratio map is useful to define the AGN-dominated region. This is because [OI] is significantly enhanced in the presence of AGNs due to the fact that [OI] becomes a more efficient coolant than [CII] in dense and warmer gas (Herrera-Camus et al. 2018). Combining this map with high-angular resolution [OIII] data, we can infer the [OIII] flux fraction of each component.

Although the origin of [OIII] emission is not clear, we try to interpret the [OIII]-to-[CII] line luminosity ratio of the two quasars. In the local Universe, based on a compiled sample of star-forming galaxies and AGN-dominated galaxies, Herrera-Camus et al. (2018) have statistically demonstrated that [OIII] becomes stronger than [CII] if galaxies have higher dust temperature. The two quasars seem to be consistent with the trend in the sense that J2054-0005 (J2310+1855) has high (low) dust temperature, $T_{\text{d}} = 50 \pm 2 \text{ K}$ ($37 \pm 1 \text{ K}$). An interpretation of the result is that J2054-0005 has a harder UV stellar radiation field than J2310+1855. Assuming the same dust covering fraction and the dust grain size distribution, a harder radiation field leads to efficient dust photoelectric heating, which in turn results in higher T_{d} (Inoue & Kamaya 2004). The harder UV radiation field would naturally enhance [OIII] (ionization potential $\approx 35 \text{ eV}$) against [CII] (ionization potential $\approx 11 \text{ eV}$) if we assume a constant C/O abundance ratio. This hypothesis can be tested with the line luminosity ratio of [NII] $205 \mu\text{m}$ against [OIII], which is a good tracer of the UV radiation hardness (Ferkinhoff et al. 2010). Alternatively, the weak [OIII] in J2310+1855 may be due to its high electron density that causes collisional de-excitation. This can be investigated with the line ratio of [OIII] $88 \mu\text{m}$ -to-[OIII] $52 \mu\text{m}$, which is sensitive to the electron density because of their different critical densities (Pereira-Santaella et al. 2017). Our results highlight the potential use of [OIII] (and the underlying continuum) as a useful tracer of the ISM in the quasar host galaxies.

Acknowledgments

This paper makes use of the following ALMA data: ADS/JAO.ALMA#2017.1.01195.S. ALMA is a partnership of ESO (representing its member states), NSF (USA) and NINS (Japan), together with NRC (Canada), NSC and ASIAA (Taiwan), and KASI (Republic of Korea), in cooperation with the Republic of Chile. The Joint ALMA Observatory is operated by ESO, AUI/NRAO and NAOJ. T.H. and A.K.I. appreciate support from NAOJ ALMA Scientific Research Grant

Number 2016-01A. We are also grateful to KAKENHI grants 26287034 and 17H01114 (K.M. and A.K.I.), 17H06130 (Y.T.). We thank Rodrigo Herrera-Camus for kindly providing us with their SHINING sample data used in the left panel of Figure 3.

References

- Bañados, E., et al. 2018, *Nature*, 553, 473
 Baldwin, J. A., Phillips, M. M., & Terlevich, R. 1981, *PASP*, 93, 5
 Beelen, A., Cox, P., Benford, D. J., Dowell, C. D., Kovács, A., Bertoldi, F., Omont, A., & Carilli, C. L. 2006, *ApJ*, 642, 694
 Bennert, N., Jungwiert, B., Komossa, S., Haas, M., & Chini, R. 2006, *A&A*, 456, 953
 Brauher, J. R., Dale, D. A., & Helou, G. 2008, *ApJS*, 178, 280
 Carniani, S., et al. 2017, *A&A*, 605, A42
 Cormier, D., et al. 2015, *A&A*, 578, A53
 da Cunha, E., et al. 2013, *ApJ*, 766, 13
 De Looze, I., et al. 2014, *A&A*, 568, A62
 De Rosa, G., et al. 2014, *ApJ*, 790, 145
 Decarli, R., et al. 2018, *ApJ*, 854, 97
 Díaz-Santos, T., et al. 2017, *ApJ*, 846, 32
 Fan, X., et al. 2003, *AJ*, 125, 1649
 Ferkinhoff, C., Hailey-Dunsheath, S., Nikola, T., Parshley, S. C., Stacey, G. J., Benford, D. J., & Staguhn, J. G. 2010, *ApJL*, 714, L147
 Feruglio, C., et al. 2018, arXiv:1804.05566
 Hashimoto, T., et al. 2018a, *Nature*, 557, 392
 Hashimoto, T., et al. 2018b, arXiv:1806.00486
 Herrera-Camus, R., et al. 2018, *ApJ*, 861, 94
 Inoue, A. K., & Kamaya, H. 2004, *MNRAS*, 350, 729
 Inoue, A. K., et al. 2016, *Science*, 352, 1559
 Izumi, T., et al. 2018, *PASJ*, 70, 36
 Jiang, L., et al. 2008, *AJ*, 135, 1057
 Jiang, L., et al. 2016, *ApJ*, 833, 222
 Kakkad, D., et al. 2018, *A&A*, 618, A6
 Kennicutt, R. C., & Evans, N. J. 2012, *ARA&A*, 50, 531
 Komatsu, E., et al. 2011, *ApJS*, 192, 18
 Kroupa, P. 2001, *MNRAS*, 322, 231
 Laporte, N., et al. 2017, *ApJL*, 837, L21
 Leipski, C., et al. 2013, *ApJ*, 772, 103
 Maiolino, R., et al. 2012, *MNRAS*, 425, L66
 Malhotra, S., et al. 1997, *ApJL*, 491, L27
 Marrone, D. P., et al. 2018, *Nature*, 553, 51
 Matsuoka, Y., et al. 2018, *ApJS*, 237, 5
 Mazzucchelli, C., et al. 2017, *ApJ*, 849, 91
 Nagao, T., Maiolino, R., Marconi, A., & Matsuhara, H. 2011, *A&A*, 526, A149
 Pereira-Santaella, M., Rigopoulou, D., Farrah, D., Lebouteiller, V., & Li, J. 2017, *MNRAS*, 470, 1218
 Priddey, R. S., & McMahon, R. G. 2001, *MNRAS*, 324, L17
 Stacey, G. J., Hailey-Dunsheath, S., Ferkinhoff, C., Nikola, T., Parshley, S. C., Benford, D. J., Staguhn, J. G., & Fiolet, N. 2010, *ApJ*, 724, 957
 Tamura, Y., et al. 2018, arXiv:1806.04132
 Valiante, R., Agarwal, B., Habouzit, M., & Pezzulli, E. 2017, *PASA*, 34, 31
 Venemans, B. P., et al. 2018, *ApJ*, 866, 159
 Wang, R., et al. 2008, *ApJ*, 687, 848
 Wang, R., et al. 2010, *ApJ*, 714, 699
 Wang, R., et al. 2013, *ApJ*, 773, 44
 Willott, C. J., Carilli, C. L., Wagg, J., & Wang, R. 2015, *ApJ*, 807, 180
 Wu, X.-B., et al. 2015, *Nature*, 518, 512
 Zhang, Z.-Y., et al. 2018, *MNRAS*, 481, 59